

# Efficient 6D Vlasov simulation using the dynamical low-rank framework **Ensign**

Fabio Cassini<sup>a,\*</sup>, Lukas Einkemmer<sup>b</sup>

<sup>a</sup>*Department of Mathematics, University of Trento, Italy*

<sup>b</sup>*Department of Mathematics, University of Innsbruck, Austria*

---

## Abstract

Running kinetic simulations using grid-based methods is extremely expensive due to the up to six-dimensional phase space. Recently, it has been shown that dynamical low-rank algorithms can drastically reduce the required computational effort, while still accurately resolving important physical features such as filamentation and Landau damping. In this paper, we propose a new second order projector-splitting dynamical low-rank algorithm for the full six-dimensional Vlasov–Poisson equations. An exponential integrator based Fourier spectral method is employed to obtain a numerical scheme that is CFL condition free but still fully explicit. The resulting method is implemented with the aid of **Ensign**, a software framework which facilitates the efficient implementation of dynamical low-rank algorithms on modern multi-core CPU as well as GPU based systems. Its usage and features are briefly described in the paper as well. The presented numerical results demonstrate that 6D simulations can be run on a single workstation and highlight the significant speedup that can be obtained using GPUs.

*Keywords:* dynamical low-rank approximation; projector-splitting integrator; Vlasov–Poisson equations; General Purpose computing on Graphic Processing Unit (GPGPU); high-dimensional PDEs; exponential integrators;

---

## 1. Introduction

Efficiently solving kinetic equations is important in applications ranging from plasma physics to radiative transport. The main challenge in this context is the up to six-dimensional phase space and the associated unfavorable scaling of computational cost and memory requirements. Assuming  $n$  discretization points for each direction of a 6D phase space, the storage cost of a direct discretization scales as  $\mathcal{O}(n^6)$ . This is usually referred to as the curse of dimensionality. To mitigate this issue, many techniques have been proposed in the literature; we mention, for example, particle methods [3, 36] and sparse grid approximations [19, 24].

---

\*Corresponding author

*Email addresses:* `fabio.cassini@unitn.it` (Fabio Cassini), `lukas.einkemmer@uibk.ac.at` (Lukas Einkemmer)

However, it is well known that the former misses or underresolves some important physical phenomena (such as Landau damping or regions with low density), while the latter has issues with the Gaussian equilibrium distribution and the low regularity inherent in collisionless kinetic problems. Because of this, direct simulations are routinely conducted on large supercomputers [1, 8]. However, current computational constraints mostly limits this to four- and some five-dimensional problems.

More recently, a dynamical low-rank algorithm for solving the Vlasov–Poisson equations has been proposed in [14]. In the context of a 6D phase space, dynamical low-rank integrators approximate the solution by a set of only three-dimensional advection problems. The resulting algorithm has the primary advantage of having storage and computational costs that scale as  $\mathcal{O}(rn^3)$  and  $\mathcal{O}(r^2n^3)$ , respectively, where  $r$  is the (usually small) rank of the approximation. This can result in a drastic reduction of both memory consumption as well as computational effort. The main enabling technology was the introduction of the projector-splitting integrator [28], which allows us to obtain a robust integrator without the need for regularization within the framework of dynamical low-rank approximations [22, 27, 29, 30].

For kinetic equations the dynamical low-rank approach offers a range of advantages, not only strictly related to storage and computational costs. For example, filamented structures in velocity space can be resolved accurately [17]. Moreover, it is known that in the linear regime [14] and for certain fluid [9, 12] and diffusive limits [7, 11] the solution has a low-rank structure, hence it is natural to use a low-rank approximation. Recently, a dynamical algorithm that is conservative from first principle has been constructed [13]. Because of these advances, dynamical low-rank approximations have received significant interest lately, and methods for problems from plasma physics [14, 17, 20, 23], radiation transport [11, 26, 32, 33], and uncertainty quantification for hyperbolic problems [25] have been proposed. These schemes have the potential to enable the 6D simulation of such systems on small clusters or even desktop computers.

While mature software packages exist for solving kinetic problems using both particle methods (e.g. [2, 35]) and methods that directly discretize the phase space on a grid (e.g. [10, 18, 34, 37]), no such software frameworks exist for dynamical low-rank algorithms. However, the need in the latter case is arguably even more critical, as the resulting evolution equations are usually somewhat more complex than the original model.

The purpose of this paper is to present six-dimensional simulations of the Vlasov–Poisson equations using the framework **Ensign**<sup>1</sup>, which facilitates the easy and efficient implementation of dynamical low-rank algorithms for kinetic equations (both on multi-core CPU and GPU based systems). In particular, we will employ a newly designed second order projector-splitting dynamical low-rank algorithm, which is based on a CFL-free (but still fully explicit) exponential integrator that uses Fourier spectral methods to compute the action of certain matrix functions. We emphasize, however, that in principle our software framework is able to support other dynamical low-rank techniques (such as the unconventional integrator [4]), and is completely flexible with regard to the specific space and time discretizations employed.

---

<sup>1</sup>Publicly available at <https://github.com/leinkemmer/Ensign> under the MIT license

In fact, almost any third party library suitable for a given problem could be used alongside **Ensign** in an implementation.

The remainder of the paper is structured as follows: in Section 2 we describe the general structure of a projector-splitting dynamical low-rank integrator for the Vlasov–Poisson equations. In Section 3 we then semi-discretize (discrete in space and continuous in time) the equations of motion resulting from the projector-splitting integrator and write them in a matrix formulation. The proposed integrator is described in detail in Section 4. In Section 5 we provide a big picture overview of the **Ensign** software framework and how it can be used to implement a dynamical low-rank algorithm. We present some numerical results in Section 6 and discuss the performance of the dynamical low-rank algorithms on CPUs and GPUs in Section 7. Finally, we conclude in Section 8.

## 2. Low-rank approximation for the Vlasov–Poisson equations

In this paper we consider the Vlasov–Poisson equations in dimensionless form given by

$$\begin{cases} \partial_t f(t, x, v) + v \cdot \nabla_x f(t, x, v) - E(f)(t, x) \cdot \nabla_v f(t, x, v) = 0, \\ E(f)(t, x) = -\nabla_x \phi(t, x), \\ -\Delta \phi(t, x) = \rho(f)(t, x) + 1, \quad \rho(f)(t, x) = -\int_{\Omega_v} f(t, x, v) dv, \end{cases} \quad (1)$$

where  $f(t, x, v)$  represents the particle-density function of the species under consideration,  $t \in \mathbb{R}_0^+$  is the time variable,  $x \in \Omega_x \subset \mathbb{R}^d$  refers to the space variable,  $v \in \Omega_v \subset \mathbb{R}^d$  is the velocity variable and  $d = 1, 2, 3$ . Depending on the physical phenomenon under study, system (1) is completed with appropriate boundary and initial conditions.

We now describe how to obtain the dynamical low-rank approximation of the Vlasov–Poisson system (1). A reader not familiar with these concepts can find more details, for instance, in [14]. The computational domain is denoted by  $\Omega = \Omega_x \times \Omega_v$ . Then, instead of directly solving system (1), we look for an approximation of the particle-density function  $f(t, x, v)$  that, for fixed  $t$ , lies in the rank- $r$  manifold

$$\mathcal{M} = \left\{ g(x, v) \in L^2(\Omega) : g(x, v) = \sum_{i,j} X_i(x) S_{ij} V_j(v) \text{ with invertible } S = (S_{ij}) \in \mathbb{R}^{r \times r}, \right. \\ \left. X_i \in L^2(\Omega_x), V_j \in L^2(\Omega_v) \text{ with } \langle X_i, X_k \rangle_x = \delta_{ik}, \langle V_j, V_\ell \rangle_v = \delta_{j\ell} \right\}$$

with corresponding tangent space

$$\mathcal{T}_f \mathcal{M} = \left\{ \dot{g}(x, v) \in L^2(\Omega) : \dot{g}(x, v) = \sum_{i,j} (X_i(x) \dot{S}_{ij} V_j(v) + \dot{X}_i(x) S_{ij} V_j(v) + X_i(x) S_{ij} \dot{V}_j(v)), \right. \\ \left. \text{with } \dot{S} \in \mathbb{R}^{r \times r}, \dot{X}_i \in L^2(\Omega_x), \dot{V}_j \in L^2(\Omega_v) \text{ and } \langle X_i, \dot{X}_k \rangle_x = 0, \langle V_j, \dot{V}_\ell \rangle_v = 0 \right\}.$$

Here  $\langle \cdot, \cdot \rangle_x$  and  $\langle \cdot, \cdot \rangle_v$  denote the standard inner products on  $L^2(\Omega_x)$  and  $L^2(\Omega_v)$ , respectively, and we employ Newton’s notation for the time derivative. Moreover, all indexes run from 1 to  $r$  and, for simplicity of presentation, we drop these limits from the notation.

To obtain the dynamical low-rank approximation of the Vlasov–Poisson system (1) we need to compute

$$\partial_t f(t, x, v) = -P(f)(v \cdot \nabla_x f(t, x, v) - E(f) \cdot \nabla_v f(t, x, v)), \quad (2)$$

where  $P(f)$  is the orthogonal projector onto the tangent space  $\mathcal{T}_f \mathcal{M}$ . For simplicity of notation, we will keep using the symbol  $f$  to denote the low-rank approximation to the particle-density. The orthogonal projection of a generic function  $g$  can be written as

$$P(f)g = P_{\nabla} g - P_{\nabla} P_{\overline{X}} g + P_{\overline{X}} g,$$

where  $P_{\overline{X}}$  and  $P_{\nabla}$  are orthogonal projectors onto the spaces spanned by the functions  $X_i$  and  $V_j$ , respectively. This formulation suggests a three-term splitting of equation (2) with subflows (in the sense of differential equations in the context of splitting schemes) given by

$$\partial_t f_1(t, x, v) = -P_{\nabla}(v \cdot \nabla_x f_1(t, x, v) - E(f_1) \cdot \nabla_v f_1(t, x, v)), \quad (3)$$

$$\partial_t f_2(t, x, v) = P_{\nabla} P_{\overline{X}}(v \cdot \nabla_x f_2(t, x, v) - E(f_2) \cdot \nabla_v f_2(t, x, v)), \quad (4)$$

$$\partial_t f_3(t, x, v) = -P_{\overline{X}}(v \cdot \nabla_x f_3(t, x, v) - E(f_3) \cdot \nabla_v f_3(t, x, v)). \quad (5)$$

This is the projector-splitting integrator that has been first proposed in [28].

By explicitly applying the projector  $P_{\nabla}$  on equation (3), we can see that solving it is equivalent to

$$\begin{cases} \partial_t K_j(t, x) = -\sum_{\ell} c_{j\ell}^1 \cdot \nabla_x K_{\ell}(t, x) + \sum_{\ell} c_{j\ell}^2 \cdot E(K)(t, x) K_{\ell}(t, x), \\ V_j(t, v) = \tilde{V}_j(v), \end{cases} \quad (6)$$

where the approximate particle-density function is written as

$$f_1(t, x, v) = \sum_j K_j(t, x) V_j(t, v), \quad K_j(t, x) = \sum_i X_i(t, x) S_{ij}(t),$$

and

$$c_{j\ell}^1 = \int_{\Omega_v} v \tilde{V}_j(v) \tilde{V}_{\ell}(v) dv, \quad c_{j\ell}^2 = \int_{\Omega_v} \tilde{V}_j(v) \nabla_v \tilde{V}_{\ell}(v) dv.$$

We refer to [14] for a more detailed derivation and a thorough explanation of the underlying mathematical structure. Equation (6) is usually referred to as the *K step* of the low-rank projector-splitting algorithm. Note that the velocity dependent low-rank factors, i.e.  $V_j$ , do not change during this step. This means that we can use their value at the beginning of the step, i.e.  $\tilde{V}_j$ , in all computations of the *K step*.

By applying both projectors  $P_{\nabla}$  and  $P_{\overline{X}}$ , the second subflow (i.e. the one related to equation (4)), can be obtained by

$$\begin{cases} \dot{S}_{ij}(t) = \sum_{k,\ell} (c_{j\ell}^1 \cdot d_{ik}^2 - c_{j\ell}^2 \cdot d_{ik}^1 [E(S)]) S_{k\ell}(t), \\ X_i(t, x) = \check{X}_i(x), \\ V_j(t, v) = \tilde{V}_j(v), \end{cases} \quad (7)$$

where

$$d_{ik}^1[E(S)] = \int_{\Omega_x} \check{X}_i(x) E(S) \check{X}_k(x) dx, \quad d_{ik}^2 = \int_{\Omega_x} \check{X}_i(x) \nabla_x \check{X}_k(x) dx.$$

We refer to equation (7) as the *S step* of the low-rank projector-splitting algorithm. Note that neither  $X_i$  nor  $V_j$  change during this step, i.e. their values are fixed to the ones at the beginning of the step ( $\check{X}_i$  and  $\check{V}_j$ , respectively).

Finally, we can demonstrate that solving equation (5) is equivalent to

$$\begin{cases} \partial_t L_i(t, v) = \sum_k d_{ik}^1[E(L)] \cdot \nabla_v L_k(t, v) - \sum_k (d_{ik}^2 \cdot v) L_k(t, v), \\ X_i(t, x) = \check{X}_i(x), \end{cases} \quad (8)$$

with the approximate particle-density function written as

$$f_3(t, x, v) = \sum_i X_i(t, x) L_i(t, v), \quad L_i(t, v) = \sum_j S_{ij}(t) V_j(t, v).$$

This step of the low-rank projector-splitting algorithm is referred to as the *L step*. Note that the  $X_i$  do not change during this step, i.e. their values are set to  $\check{X}_i$ .

Concerning the equations of the electric field, they can be written in terms of the low-rank factors  $X_i(t, x)$ ,  $S_{ij}(t)$  and  $V_j(t, v)$  as well. Indeed, depending on the need, we can express the charge density  $\rho(f)(t, x)$  as

$$\begin{aligned} \rho(K)(t, x) &= - \sum_j K_j(t, x) \rho(\check{V}_j(v)), & \rho(\check{V}_j(v)) &= \int_{\Omega_v} \check{V}_j(v) dv, \\ \rho(S)(t, x) &= - \sum_{i,j} \check{X}_i(x) S_{ij}(t) \rho(\check{V}_j(v)), \\ \rho(L)(t, x) &= - \sum_i \check{X}_i(x) \rho(L_i(t, v)), & \rho(L_i(t, v)) &= \int_{\Omega_v} L_i(t, v) dv, \end{aligned}$$

where the relevant quantities are defined above.

Finally, the approximate solution to the Vlasov–Poisson equations, i.e. system (1), is obtained by combining the partial solutions of the *K*, *S* and *L* step in a splitting fashion. In the easiest setting, the first order Lie splitting scheme concatenates the three subflows in sequence, see Section 3.1. We will also outline a second order scheme based on Strang splitting in Section 3.2.

### 3. Matrix formulation of the semi-discrete algorithm

So far we have considered the low-rank approximation in a continuous framework. However, to perform calculations on a computer we have to discretize the equations for the *K*, *S*, and *L* steps. In this section, we assume that a space discretization has been chosen. Our goal is then to collect the degrees of freedom into matrices and vectors and write the

resulting equations as operations on those objects. The implementation using the software framework **Ensign**, described later in Section 5, is also based on this formulation.

We consider  $n_{x_k}$  discretization points for the space variable  $x_k$ ,  $k = 1, \dots, d$  and  $n_{v_k}$  discretization points for the velocity variable  $v_k$ ,  $k = 1, \dots, d$ . The total numbers of degrees of freedom are denoted as  $N_x = n_{x_1} \cdots n_{x_d}$  and  $N_v = n_{v_1} \cdots n_{v_d}$  for space and velocity, respectively. Then, for a fixed time  $t$ , we define  $X = [X_1, \dots, X_r] \in \mathbb{R}^{N_x \times r}$  to be the matrix having as columns the evaluation of the low-rank factors  $X_i$  at the chosen spatial grid. Clearly, the resulting matrix entries depend on the discretization performed and on the ordering of the grid points. Similarly, we consider  $V = [V_1, \dots, V_r] \in \mathbb{R}^{N_v \times r}$  to be the matrix having as columns the evaluation of the low-rank factors  $V_j$  at the velocity grid. The coupling coefficients  $S_{ij}$  are collected in the matrix  $S \in \mathbb{R}^{r \times r}$ . Hence, we can write the evolution equation for the  $K$  step (6) in matrix formulation as follows

$$\partial_t K(t) = - \sum_{i=1}^d \bar{\partial}_{x_i} K(t) C_{1,v_i}^\top + \sum_{i=1}^d \text{diag}(E_{x_i}(K(t))) K(t) C_{2,v_i}^\top, \quad (9)$$

where

$$\begin{aligned} K(t) &= X(t)S(t), \quad K(t) \in \mathbb{R}^{N_x \times r}, \\ C_{1,v_i} &= \tilde{V}^\top \text{diag}(\omega_{1,v_i}) \tilde{V} \in \mathbb{R}^{r \times r}, \\ C_{2,v_i} &= \tilde{V}^\top \text{diag}(\omega_{2,v_i}) \bar{\partial}_{v_i} \tilde{V} \in \mathbb{R}^{r \times r}, \end{aligned}$$

and  $\omega_{1,v_i}$  and  $\omega_{2,v_i}$  are suitable quadrature weights. The  $i$ th component of the electric field has been denoted by  $E_{x_i}(K(t)) \in \mathbb{R}^{N_x}$ . In addition, we have used  $\bar{\partial}_{x_i}$  to denote the discretization of the spatial derivative operator. While this operator can be represented as a matrix, in many cases it is more efficient to directly compute its application to  $K(t)$  (e.g. in a stencil code or by using FFTs). We also note that in order to compute the coefficients  $C_{1,v_i}$  and  $C_{2,v_i}$  it would (obviously) be very inefficient to form the diagonal matrix. Instead, our framework **Ensign** provides the function `coeff` that takes the matrices as well as a vector of weights as input and computes the corresponding quadrature (see Section 5 for more details).

For the evolution equation of the  $S$  step (7) we obtain

$$\dot{S}(t) = \sum_{i=1}^d D_{2,x_i} S(t) C_{1,v_i}^\top - \sum_{i=1}^d D_{1,x_i} [E(S(t))] S(t) C_{2,v_i}^\top, \quad (10)$$

where

$$\begin{aligned} D_{1,x_i} [E(S(t))] &= \check{X}^\top \text{diag}(\omega_{1,x_i}^E) \check{X} \in \mathbb{R}^{r \times r}, \\ D_{2,x_i} &= \check{X}^\top \text{diag}(\omega_{2,x_i}) \bar{\partial}_{x_i} \check{X} \in \mathbb{R}^{r \times r}, \end{aligned}$$

and again  $\omega_{1,x_i}^E$  and  $\omega_{2,x_i}$  are suitable quadrature weights.

Finally, for the evolution equation of the  $L$  step (8) we have

$$\partial_t L(t) = \sum_{i=1}^d \bar{\partial}_{v_i} L(t) D_{1,x_i}^\top - \sum_{i=1}^d \text{diag}(\bar{v}_i) L(t) D_{2,x_i}^\top, \quad (11)$$

where

$$L(t) = V(t)S(t)^\top, \quad L(t) \in \mathbb{R}^{N_v \times r},$$

and  $\bar{v}_i \in \mathbb{R}^{N_v}$  is the vector with the positions of the grid points in velocity space.

In matrix formulation, the equations for the electric field are given by

$$\begin{aligned} (E_{x_1}(f)(t), \dots, E_{x_d}(f)(t)) &= -\bar{\nabla}_x \Phi(f)(t), \quad E_{x_i}(f)(t) \in \mathbb{R}^{N_x}, \quad \Phi(f)(t) \in \mathbb{R}^{N_x}, \\ -\bar{\Delta} \Phi(f)(t) &= P(f)(t) + 1, \quad P(f)(t) \in \mathbb{R}^{N_x}, \end{aligned}$$

where the discretized charge density  $P(f)(t)$  can be computed in terms of the low-rank factors, depending on the need, as

$$P(K)(t) = -K(t)\tilde{P}, \quad \tilde{P} = \tilde{V}^\top \omega_v \in \mathbb{R}^r, \quad \omega_v \in \mathbb{R}^{N_v}, \quad (12)$$

$$P(S)(t) = -\check{X}S(t)\tilde{P},$$

$$P(L)(t) = -\check{X}\bar{P}(L(t)), \quad \bar{P}(L(t)) = L(t)^\top \omega_v \in \mathbb{R}^r. \quad (13)$$

Here  $\omega_v$  is a vector which collects suitable quadrature weights.

Let us also note that the approximation of the particle-density function can be recovered at any moment from the low-rank factors by computing

$$F(t) = X(t)S(t)V(t)^\top \in \mathbb{R}^{N_x \times N_v},$$

but clearly this is not needed for the low-rank projector-splitting algorithm, and doing so would be extremely costly.

### 3.1. Order 1 low-rank projector-splitting algorithm

The subflows corresponding to the  $K$  step, the  $S$  step, and the  $L$  step are then combined by a splitting scheme in order to recover an approximation of the particle-density function. For a first order method it is clearly sufficient to consider a Lie–Trotter splitting algorithm. A detailed description of the resulting scheme is given in Algorithm 1.

Remark that the computation of the electric field is performed only once at the beginning of the time step. This is not a restriction in the context of a Lie–Trotter splitting, as fixing the electric field at each time step still results in a first order approximation. In principle, any numerical method can be employed to integrate in time equations (9)–(11). We will discuss our proposal, based on the choice of a spectral phase space discretization, in Section 4. Moreover, after performing the  $K$  and the  $L$  steps, in order to proceed with the algorithm we need to recover the orthonormal functions  $X_i$ ,  $V_j$  and the coupling coefficients  $S_{ij}$ . This can be accomplished, for example, by a QR or an SVD decomposition. Finally, we note that overall storage and computational costs of the dynamical low-rank algorithm, for  $n_{x_i} = n_{v_i} = n$ , scale as  $\mathcal{O}(rn^d)$  and  $\mathcal{O}(r^2n^d)$ , respectively. For more details we refer the reader to [14].

---

**Algorithm 1:** First order dynamical low-rank integrator for the Vlasov–Poisson equations (1).

---

**Input:**  $X^0, S^0, V^0$  such that  $f(0, x, v) \approx \sum_{i,j} X_i^0(x) S_{ij}^0 V_j^0(v)$ , time step size  $\tau$

**Output:**  $X^1, S^3, V^1$  such that  $f(\tau, x, v) \approx \sum_{i,j} X_i^1(x) S_{ij}^3 V_j^1(v)$

- 1 Compute  $C_{1,v_i}$  and  $C_{2,v_i}$ ,  $i = 1, \dots, d$ , using  $V^0$ ;
  - 2 Compute  $K^0$  using  $X^0$  and  $S^0$ ;
  - 3 Compute the electric field  $E^0$  with equation (12) using  $K^0$  and  $V^0$ ;
  - 4 Solve equation (9) with initial value  $K^0$  and  $E^0$  up to time  $\tau$  to obtain  $K^1$ ;
  - 5 Perform a QR decomposition of  $K^1$  to obtain  $X^1$  and  $S^1$ ;
  - 6 Compute  $D_{1,x_i}$  and  $D_{2,x_i}$ ,  $i = 1, \dots, d$ , using  $E^0$  and  $X^1$ ;
  - 7 Solve equation (10) with initial value  $S^1$  and  $E^0$  up to time  $\tau$  to obtain  $S^2$ ;
  - 8 Compute  $L^0$  using  $V^0$  and  $S^2$ ;
  - 9 Solve equation (11) with initial value  $L^0$  and  $E^0$  up to time  $\tau$  to obtain  $L^1$ ;
  - 10 Perform a QR decomposition of  $L^1$  to obtain  $V^1$  and  $S^3$ ;
- 

### 3.2. Order 2 low-rank projector-splitting algorithm

A straightforward generalization to a second order integrator by employing a Strang splitting procedure instead of a Lie–Trotter one is not possible. Indeed, if we freeze the electric field at the beginning of the time step, we still end up with a first order algorithm. To overcome this problem, an almost symmetric Strang splitting scheme is proposed in [14]; however, in order to achieve full second order, that algorithm requires several updates of the electric field, which in turn translates into high computational effort. We propose here a slightly different strategy to obtain a second order scheme, listed in detail in Algorithm 2. The underlying idea is that we compute an approximation of the electric field at time  $\tau/2$  of (local) second order by means of Algorithm 1. Then, we restart the integration with a classic Strang splitting scheme employing as constant electric field the approximation at the half step. Mathematically, this can still be analyzed as an almost symmetric splitting scheme (see [15, 16]), and as for Algorithm 1 the storage and computational costs scale as  $\mathcal{O}(rn^d)$  and  $\mathcal{O}(r^2n^d)$ , respectively.



---

**Algorithm 2:** Second order dynamical low-rank integrator for the Vlasov–Poisson equations (1).

---

**Input:**  $X^0, S^0, V^0$  such that  $f(0, x, v) \approx \sum_{i,j} X_i^0(x) S_{ij}^0 V_j^0(v)$ , time step size  $\tau$

**Output:**  $X^3, S^7, V^1$  such that  $f(\tau, x, v) \approx \sum_{i,j} X_i^3(x) S_{ij}^7 V_j^1(v)$

- 1 Perform steps 1–9 of Algorithm 1 with time step size  $\tau/2$ ;
  - 2 Compute the electric field  $E^{1/2}$  with equation (13) using  $X^1$  and  $L^1$  from step 1.;
  - 3 Solve equation (9) with initial value  $K^0$  and  $E^{1/2}$  up to time  $\tau/2$  to obtain  $K^2$ ;
  - 4 Perform a QR decomposition of  $K^2$  to obtain  $X^2$  and  $S^3$ ;
  - 5 Compute  $D_{1,x_i}$  and  $D_{2,x_i}$ ,  $i = 1, \dots, d$ , using  $E^{1/2}$  and  $X^2$ ;
  - 6 Solve equation (10) with initial value  $S^3$  and  $E^{1/2}$  up to time  $\tau/2$  to obtain  $S^4$ ;
  - 7 Compute  $L^1$  using  $V^0$  and  $S^4$ ;
  - 8 Solve equation (11) with initial value  $L^1$  and  $E^{1/2}$  up to time  $\tau$  to obtain  $L^2$ ;
  - 9 Perform a QR decomposition of  $L^2$  to obtain  $V^1$  and  $S^5$ ;
  - 10 Compute  $C_{1,v_i}$  and  $C_{2,v_i}$ ,  $i = 1, \dots, d$ , using  $V^1$ ;
  - 11 Solve equation (10) with initial value  $S^5$  and  $E^{1/2}$  up to time  $\tau/2$  to obtain  $S^6$ ;
  - 12 Compute  $K^3$  using  $X^2$  and  $S^6$ ;
  - 13 Solve equation (9) with initial value  $K^3$  and  $E^{1/2}$  up to time  $\tau/2$  to obtain  $K^4$ ;
  - 14 Perform a QR decomposition of  $K^4$  to obtain  $X^3$  and  $S^7$ ;
- 

#### 4. Time and space discretization of $K$ , $S$ and $L$ steps

As already mentioned in Section 3, in principle any numerical scheme can be used to integrate in time equations (9)–(11). However, depending on the selected phase-space discretization, some choices can be more adequate than others. In particular, we describe here in detail an exponential integrator based strategy which uses a Fourier spectral discretization for both space and velocity variables. The method converges rapidly in space and velocity (owing to the spectral discretization) and despite being fully explicit does not suffer from a CFL induced step size restriction in time.

Let us consider the  $K$  step (9). As we are interested in performing 6D simulations, for clarity of exposition we will only consider the case  $d = 3$  here. The (simpler) cases  $d = 1$  and  $d = 2$  can be treated similarly. Then, by performing a further splitting of the  $K$  step we obtain the following three equations

$$\partial_t K_1(t) = -\bar{\partial}_{x_1} K_1(t) C_{1,v_1}^\top, \quad (14)$$

$$\partial_t K_2(t) = -\bar{\partial}_{x_2} K_2(t) C_{1,v_2}^\top, \quad (15)$$

$$\partial_t K_3(t) = -\bar{\partial}_{x_3} K_3(t) C_{1,v_3}^\top + \sum_{i=1}^3 \text{diag}(E_{x_i}) K_3(t) C_{2,v_i}^\top. \quad (16)$$

Note that, in principle, the summation term related to the electric field could be put in any of the three equations (14)–(16), without any substantial change. On the other hand, in a general setting, there would not be advantages in treating this term in a separate

flow, because there is no exact solution in Fourier space and more splitting error would be generated.

Applying then a Fourier transform in the  $x_i$  variables (denoted by  $\mathcal{F}_{x_i}$ ) we obtain

$$\begin{aligned}\partial_t \hat{K}_1(t) &= -D_{x_1}^{\mathcal{F}} \hat{K}_1(t) C_{1,v_1}^{\top}, \\ \partial_t \hat{K}_2(t) &= -D_{x_2}^{\mathcal{F}} \hat{K}_2(t) C_{1,v_2}^{\top}, \\ \partial_t \hat{K}_3(t) &= -D_{x_3}^{\mathcal{F}} \hat{K}_3(t) C_{1,v_3}^{\top} + \sum_{i=1}^3 \mathcal{F}_{x_3}(\text{diag}(E_{x_i}) K_3(t)) C_{2,v_i}^{\top},\end{aligned}$$

where  $\hat{K}_i(t) = \mathcal{F}_{x_i}(K_i(t))$  and  $D_{x_i}^{\mathcal{F}}$  is a diagonal matrix containing the coefficients stemming from the differential operator  $\bar{\partial}_{x_i}$  in Fourier space. Then, as the matrices  $C_{1,v_i}^{\top}$  are symmetric by construction, it is possible to diagonalize them so that  $C_{1,v_i}^{\top} = T_{v_i} D_{v_i} T_{v_i}^{\top}$ . We note that this operation is computationally cheap as the matrices involved have only size  $r \times r$ . By performing the substitution  $\hat{M}_i(t) = \hat{K}_i(t) T_{v_i}$  we have

$$\partial_t \hat{M}_1(t) = -D_{x_1}^{\mathcal{F}} \hat{M}_1(t) D_{v_1}, \quad (17)$$

$$\partial_t \hat{M}_2(t) = -D_{x_2}^{\mathcal{F}} \hat{M}_2(t) D_{v_2}, \quad (18)$$

$$\partial_t \hat{M}_3(t) = -D_{x_3}^{\mathcal{F}} \hat{M}_3(t) D_{v_3} + \sum_{i=1}^3 \mathcal{F}_{x_3}(\text{diag}(E_i) K_3(t)) C_{2,v_i}^{\top} T_{v_3}. \quad (19)$$

At this point, equations (17) and (18) can be solved exactly in time by means of independent pointwise operations, while equation (19) can be solved efficiently by means of a first or second order exponential Runge–Kutta method (see [21] for a survey), again just using independent pointwise operations. We choose to use exponential integrators in the time evolution of this step because in this way we remove any CFL-like restriction of the step size coming from the stiffness of the spatial derivative. Moreover, as everything is written in terms of independent pointwise operations, the computation of the single flow can be performed completely in parallel.

Finally, coming back to the original variables  $\hat{K}_i$  and performing an inverse Fourier transform, we obtain approximate solutions for the equations involved. Embedding this procedure in a splitting context returns the desired approximation of the evolution equation for the  $K$  step. In particular, for the first order method described in Algorithm 1 it is enough to perform a Lie–Trotter splitting, while a (classical) Strang splitting procedure is needed for the second order method presented in Algorithm 2.

Concerning the integration of the evolution equation of the  $L$  step (11), similar considerations apply. Finally, concerning the  $S$  step (10), it is an  $r \times r$  problem and there is no source of stiffness in it. Hence, we perform its time integration by means of the classical explicit fourth order Runge–Kutta scheme RK4. In principle it would be sufficient to use a first order scheme, in the context of Algorithm 1, and a second order scheme, in the context of Algorithm 2. However, since the  $S$  step is cheap, we can use a higher order approximation at negligible additional computational cost and reduce the error term associated with integrating  $S$  from the numerical scheme.

## 5. The Ensign framework and implementation

As presented in Sections 2–4, in the context of dynamical low-rank algorithms a function  $f(t, x, v)$  is approximated as  $f(t, x, v) \approx \sum_{i,j} X_i(t, x) S_{ij}(t) V_j(t, v)$ , where the indexes  $i$  and  $j$  run from 1 to  $r$  and  $r$  is the chosen approximation rank. The quantities  $X_i(t, x)$ ,  $S_{ij}(t)$  and  $V_j(t, v)$  constitute the so called low-rank factors and, after discretization in  $x$  and  $v$ , they can be expressed as matrices, allowing us to write the scheme in matrix formulation. Therefore, independently of the specific case under consideration, the common key point for an efficient implementation of dynamical low-rank algorithms for kinetic equations, both on CPU and GPU based systems, is the fast computation of operations on matrices and vectors (e.g. matrix-matrix and matrix-vector products, certain pointwise operations, etc). For every modern computer architecture, we have at our disposal heavily optimized routines to perform such operations, usually referred to as BLAS. For example, Intel MKL [5] and OpenBLAS [38] are available for CPU based systems while we have cuBLAS [6] and MAGMA [31] for NVIDIA GPUs. Among their many features, all these libraries are equipped with multithreaded versions of BLAS routines. When possible we use these libraries heavily. However, we note that there are certain operations that we need to perform in the context of a low-rank algorithm that are not part of BLAS.

The main idea behind **Ensign** is to provide the user a collection of structures and functions in order to compute and manipulate *easily* the arising quantities in dynamical low-rank algorithms. Let us note that our goal here is to provide primitives that allow the user to implement dynamical low-rank approximations on a high-level. Thus, we are concerned with relevant data structures for dynamical low-rank algorithms, for computing the coefficients that appear in the approximations (which can have, in general, two or more indices and also spatial dependences), for performing certain operations such as initialization, addition or truncation on low-rank approximations, orthogonalization with respect to arbitrary inner products, and writing such low-rank approximations to disk. This could then be complemented by the user of **Ensign** with libraries that perform spatial and temporal discretization. Our framework is written in C++ programming language and uses CUDA internally for the GPU code.

We now illustrate some of its features with the aid of the first order projector-splitting dynamical low-rank algorithm presented in Section 3.1, assuming an underlying six-dimensional phase space. To this aim, in Figure 1 we translate in source code some lines of the pseudocode of Algorithm 1, and in Figure 2 we show how it is possible to initialize the low-rank factors. We can immediately note how the quantities arising from the mathematical equations can be naturally translated into the structures and functions provided by our framework. In particular, in terms of data storage we employ a structure `multi_array` which lets us easily define vectors (`w1v1`, for example) and matrices (`C1v1`, for example) both in CPU and in GPU memory, depending on the need. This structure is also enriched with some user-friendly functions and operators which are useful to perform basic operations between `multi_arrays`, such as sum, difference, multiplication with a scalar, and to transfer data from/to CPU/GPU memory (the latter can be simply done by assignment, as commented in Figure 2). For convenience of the user, we provide also a structure `lr2`, which contains

three 2D `multi_arrays` (`X`, `S` and `V`) that reflect the evaluation of the low-rank factors on a discretized grid and their coupling coefficients. In particular, the degrees of freedom are linearized so that each column corresponds to the discretized version of a single low-rank factor. While the specific example of Figure 2 is presented in the context of a uniform space discretization, any other kind of discretization (with an arbitrary ordering of the nodes) would work in a straightforward way as well.

We use C++ templates in order to abstract the underlying architecture on which the code is run. Depending on whether a function is called with arguments that reside on the CPU or on the GPU, an efficient implementation suitable for that hardware architecture is selected. Indeed, whether the code runs on the CPU or on the GPU is never explicitly specified in the code example in Figure 1, because it is automatically detected from the storage location of the input arguments of the functions. Thus, the algorithmic part of the implementation is completely independent of what computer hardware the code is eventually run on.

Concerning BLAS operations, `Ensign` provides the structure `blas_ops` which contains wrappers for matrix multiplications (e.g. `matmul` and `matmul_transb`) and handles needed to call properly these routines on the GPU. Then, our framework is equipped with a function to compute the  $C$  and  $D$  integral coefficients, namely `coeff`. Depending on the input matrices and the vector of weights, the function computes the corresponding matrix of coefficients. As an example, given the 1D quadrature weight `multi_array w1v1` and the 2D `multi_array lr_st.V`, the coefficient matrix  $C_{1,v_1}$  can be computed using the command in line 8 of the code in Figure 1. Also, we can find in our framework the structure `gram_schmidt`, which contains a function to compute the QR decomposition of a matrix with a generic inner product. It is based on a modified Gram-Schmidt algorithm written as much as possible in matrix formulation, so that again the internal computations are automatically performed in parallel by means of calls to appropriate BLAS. Modified Gram-Schmidt is used here because it is easy to parallelize and can operate purely in terms of inner products, even if the associated degrees of freedom are not stored directly as a vector. The latter is important in the case of hierarchical low-rank approximations such as the those considered in [14]. For example, given the 2D `multi_arrays lr_st.X` and `lr_st.S` and the inner product `ip_xx`, the call to perform the QR decomposition of `lr_st.X` is given in line 22 of Figure 1.

Finally, we want to emphasize that while we have illustrated our software framework for a simple projector-splitting based dynamical low-rank integrator, every effort has been made in designing `Ensign` to allow also the implementation of other dynamical low-rank integrators, such as the recently proposed unconventional integrator [4] or the conservative dynamical low-rank integrator [13]. Moreover, we again point out that the user is completely free to choose any space or time discretization appropriate to the problem. The only requirement in terms of space discretization is that the degrees of freedom of the low-rank factors have to be collected in suitable matrices by means of an index linearization. This is certainly possible for all the commonly used space discretization strategies.

```

1 // Declaration and initialization
2 /* See Figure 2 */
3 gram_schmidt gs(&blas);
4 multi_array<double,1> w1v1(stloc::host); // stloc::device if on GPU
5 multi_array<double,2> C1v1(stloc::host);
6 /* ... */
7 // Line 1: Compute C coefficients
8 coeff(lr_st.V, lr_st.V, w1v1, C1v1, blas);
9 coeff(lr_st.V, lr_st.V, w1v2, C1v2, blas);
10 coeff(lr_st.V, lr_st.V, w1v3, C1v3, blas);
11 coeff(lr_st.V, dV0_v1, w2v1, C2v1, blas);
12 coeff(lr_st.V, dV0_v2, w2v2, C2v2, blas);
13 coeff(lr_st.V, dV0_v3, w2v3, C2v3, blas);
14 // Line 2: Compute K0
15 tmpX = lr_st.X;
16 blas.matmul(tmpX, lr_st.S, lr_st.X);
17 // Line 3: Compute electric field
18 /* ... */
19 // Line 4: Solve K step
20 /* ... */
21 // Line 5: Perform QR decomposition
22 gs(lr_st.X, lr_st.S, ip_xx);
23 /* ... */
24 // Line 6: Compute D coefficients
25 coeff(lr_st.X, lr_st.X, wE1x1, D1x1, blas);
26 coeff(lr_st.X, lr_st.X, wE1x2, D1x2, blas);
27 coeff(lr_st.X, lr_st.X, wE1x3, D1x3, blas);
28 coeff(lr_st.X, dX1_x1, w2x1, D2x1, blas);
29 coeff(lr_st.X, dX1_x2, w2x2, D2x2, blas);
30 coeff(lr_st.X, dX1_x3, w2x3, D2x3, blas);
31 // Line 7: Solve S step
32 /* ... */
33 // Line 8: Compute L0
34 tmpV = lr_st.V;
35 blas.matmul_transb(tmpV, lr_st.S, lr_st.V);
36 // Line 9: Solve L step
37 /* ... */
38 // Line 10: Perform QR decomposition
39 gs(lr_st.V, lr_st.S, ip_vv);
40 transpose_inplace(lr_st.S);

```

Figure 1: Sketch of a C++ implementation of Algorithm 1 using the **Ensign** framework. To perform computation on the GPU, it is enough to use `d_lr_st` instead of `lr_st`, and to declare the relevant `multi_arrays` with `stloc::device`. The syntax `/*...*/` indicates code not reported for simplicity of exposition.

```

1  typedef ptrdiff_t Index;
2  array<Index,3> N_xx, N_vv;
3  array<double,3> lim_xx, lim_vv, h_xx, h_vv;
4  Index r;
5  blas_ops blas;
6  vector<const double*> X0, V0;
7
8  // Initialize N_xx, lim_xx, h_xx, N_vv, lim_vv, h_vv and r on CPU
9  /* ... */
10
11 Index N_xx_m = N_xx[0]*N_xx[1]*N_xx[2];
12 Index N_vv_m = N_vv[0]*N_vv[1]*N_vv[2];
13
14 // Define inner products that are used in the algorithm
15 auto ip_xx = inner_product_from_const_weight(h_xx[0]*h_xx[1]*h_xx
16 [2], N_xx_m);
17 auto ip_vv = inner_product_from_const_weight(h_vv[0]*h_vv[1]*h_vv
18 [2], N_vv_m);
19
20 // Initialize the low-rank structure for the initial value
21 // (the initial value is given by X0 and V0 and can usually
22 // be easily determined from the problem)
23 // To illustrate data movement (see below) we perform the
24 // initialization on the CPU and then transfer the result
25 // to the GPU.
26
27 lr2<double> lr_st(r,{N_xx_m,N_vv_m});
28
29 // Set up X0 and V0
30 /* ... */
31
32 initialize(lr_st, X0, V0, ip_xx, ip_vv, blas);
33
34 // Assignment of two lr2 or multi_arrays copies from CPU to GPU
35 lr2<double> d_lr_st(r,{N_xx_m,N_vv_m},stloc::device); // on GPU
36 d_lr_st = lr_st;

```

Figure 2: Sketch of a C++ implementation for the initialization of low-rank factors using the Ensign framework.  $N_{xx}$ ,  $lim_{xx}$  and  $h_{xx}$  are arrays which contain the number of discretization points, the left extremes of the space domain and the grid spacing for each direction, respectively (similarly for  $N_{vv}$ ,  $lim_{vv}$  and  $h_{vv}$ , which are related to the velocity domain).  $r$  is the approximation rank, while  $lr\_st$  and  $d\_lr\_st$  are structures which contain 2D `multi_arrays` that reside on the CPU and on the GPU, respectively. The syntax `/*...*/` indicates code not reported for simplicity of exposition.

## 6. Numerical experiments

In this section we will present some numerical results and validate the implementations of the algorithms described in Section 3. The developed code solves the 6D Vlasov–Poisson equations (1) and uses the framework **Ensign**. All the experiments in this section have been performed in double precision arithmetic with the aid of a single NVIDIA Tesla A100 card (theoretical peak memory bandwidth of 1555 GB/s and peak floating point processing power for double precision of 9.7 TFlops), equipped with 40 GB of RAM.

### 6.1. Orders of convergence

First of all, we check the implementation of the low-rank projector-splitting algorithms by computing numerically the order of convergence of the methods. To this purpose, we consider a 6D linear Landau problem posed on the domain  $\Omega = (0, 4\pi)^3 \times (-6, 6)^3$  with an initial particle-density given by

$$f_0(x_1, x_2, x_3, v_1, v_2, v_3) = \frac{1}{\sqrt{(2\pi)^3}} e^{-(v_1^2 + v_2^2 + v_3^2)/2} (1 + \alpha_1 \cos(\kappa_1 x_1) + \alpha_2 \cos(\kappa_2 x_2) + \alpha_3 \cos(\kappa_3 x_3)). \quad (20)$$

The parameters are set to  $\alpha_1 = \alpha_2 = \alpha_3 = 10^{-2}$  and  $\kappa_1 = \kappa_2 = \kappa_3 = \frac{1}{2}$ . We consider the problem with periodic boundary conditions in all directions and integrate it up to final time  $T = 1$ . Concerning the space discretization, we take  $32^3$  as number of discretization points for both space and velocity variables. The rank of the solution is fixed to  $r = 10$ . As a reference solution, we take the result of the second order low-rank projector-splitting algorithm with  $m = 2000$  time steps (time step size  $\tau = 5 \cdot 10^{-4}$ ).

We also consider a 6D two stream instability problem defined on the domain  $\Omega = (0, 10\pi)^3 \times (-9, 9)^3$  with initial distribution

$$\begin{aligned} f_0(x_1, x_2, x_3, v_1, v_2, v_3) &= \frac{1}{\sqrt{(8\pi)^3}} \left( e^{-(v_1 - \bar{v}_1)^2/2} + e^{-(v_1 - \tilde{v}_1)^2/2} \right) \\ &\quad \times \left( e^{-(v_2 - \bar{v}_2)^2/2} + e^{-(v_2 - \tilde{v}_2)^2/2} \right) \\ &\quad \times \left( e^{-(v_3 - \bar{v}_3)^2/2} + e^{-(v_3 - \tilde{v}_3)^2/2} \right) \\ &\quad \times (1 + \alpha_1 \cos(\kappa_1 x_1) + \alpha_2 \cos(\kappa_2 x_2) + \alpha_3 \cos(\kappa_3 x_3)). \end{aligned} \quad (21)$$

In this case the parameters are given by  $\alpha_1 = \alpha_2 = \alpha_3 = 10^{-3}$ ,  $\kappa_1 = \kappa_2 = \kappa_3 = \frac{1}{5}$ ,  $\bar{v}_1 = \frac{5}{2}$ ,  $\bar{v}_2 = \bar{v}_3 = 0$ ,  $\tilde{v}_1 = -\frac{5}{2}$ ,  $\tilde{v}_2 = -\frac{9}{4}$  and  $\tilde{v}_3 = -2$ . As for linear Landau damping, the problem is equipped with periodic boundary conditions in all directions and the rank is fixed to  $r = 10$ . We perform simulations up to final time  $T = \frac{1}{20}$  with  $32^3$  discretization points for both space and velocity variables. We again consider as a reference solution the results of the second order algorithm with  $m = 2000$  time steps (time step size  $\tau = 2.5 \cdot 10^{-5}$ ).

The results for both problems are collected in Figure 3. In each of the two cases, we can clearly see that the first and second order algorithms show the expected order of convergence.

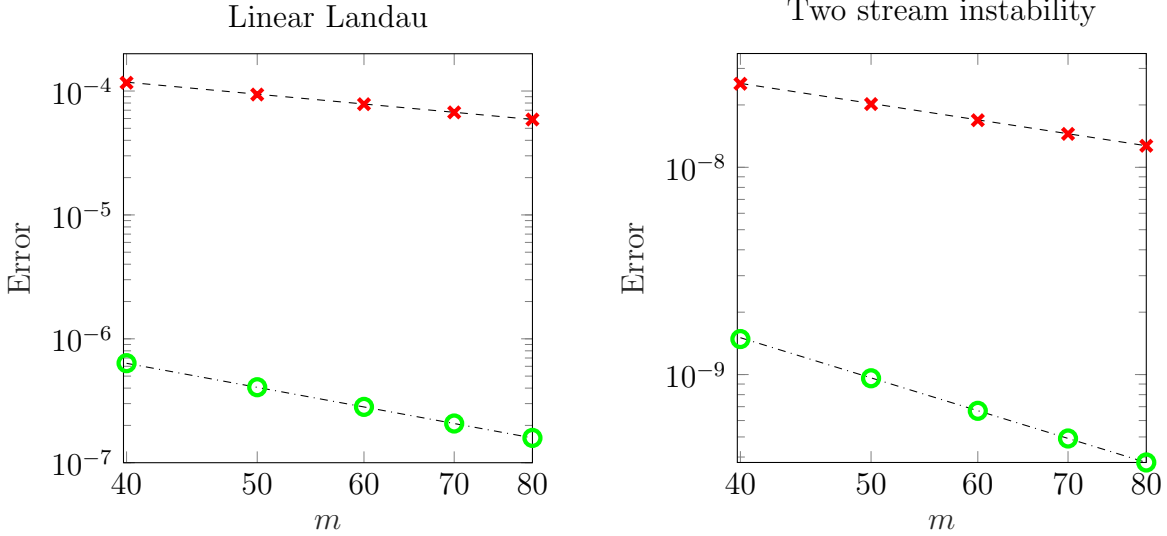


Figure 3: Orders of convergence for first order (red crosses) and second order (green circles) low-rank projector-splitting algorithms 1 and 2. Left plot: linear Landau damping (20) with  $T = 1$ . Right plot: two stream instability problem (21) with  $T = \frac{1}{20}$ . In both cases, the rank is set to  $r = 10$ . The (relative) error is computed in maximum norm at the final time for a number of time steps equal to  $m = 40, 50, 60, 70, 80$ , with respect to a reference solution produced with Algorithm 2 and  $m = 2000$  time steps. The dashed and dashed-dotted lines are reference lines of slope -1 and -2, respectively.

### 6.2. Linear Landau simulation

We consider again the 6D linear Landau problem (20) with periodic boundary conditions and the same set of parameters. However, now we pick  $64^3$  discretization points for the space variables and  $256^3$  for the velocity ones. The approximation rank is fixed to  $r = 10$ , and we perform two simulations with time step sizes  $\tau = 10^{-1}$  and  $\tau = 10^{-2}$ , respectively. We emphasize that a direct (Eulerian or semi-Lagrangian) Vlasov solver would require a total number of degrees of freedom of approximately  $4.4 \cdot 10^{12}$ , and at least 70 TB of main memory (RAM) to perform the simulations in double precision arithmetic. This would clearly only be feasible on a supercomputer. Our dynamical low-rank simulation, in contrast, runs on a single NVIDIA A100 equipped with 40 GB of memory, and the number of degrees of freedom are  $10 \cdot 64^3 + 10 \cdot 256^3 \approx 1.7 \cdot 10^8$ . The computational time of execution is approximately six minutes for the simulation with  $\tau = 10^{-1}$  and an hour for the one with  $\tau = 10^{-2}$ .

The results obtained, in terms of electric energy, error in mass and error in total energy, are summarized in Figure 4. We can observe that the electric energy shows the expected theoretical exponential rate of decay up to approximately  $10^{-6}$ , with very similar results for both the time step sizes. In this sense, what dominates after time  $t = 40$  is the low-rank error, and we basically enter into a stagnation region (see Section 7.2 and Figure 6 for simulations with higher ranks). Concerning the errors in mass and in total energy (both quantities are conserved by the original equations), even though the proposed low-rank projector-splitting integrator does not preserve a priori any quantity we obtain conservation of mass up to roughly  $3 \cdot 10^{-8}$  and up to  $7 \cdot 10^{-7}$  or  $4 \cdot 10^{-8}$  for the energy, depending on the time step size.



In this sense, the simulation with smaller time step size produces better results, meaning that for these quantities we still did not encounter a bound stemming from the low-rank truncation.

### 6.3. Two stream instability simulation

Let us perform now two simulations with the 6D two stream instability problem (21) and  $128^3$  discretization points for both spatial and velocity variables. The set of parameters is the same as for the example presented in Section 6.1, but we integrate the problem until time  $T = 60$  with the second order algorithm 2 and time step sizes  $\tau = 6 \cdot 10^{-2}$  and  $\tau = 10^{-2}$ . The rank is fixed to  $r = 10$ . Again, a direct Vlasov solver would require a total number of degrees of freedom of approximately  $4.4 \cdot 10^{12}$ , while the dynamical low rank approach has  $2 \cdot 10 \cdot 128^3 \approx 4.2 \cdot 10^7$  degrees of freedom. As for the linear Landau problem, we investigate the behavior of the electric energy and the conservation of mass and total energy. The results are summarized in Figure 5. In both cases, as expected, the electric energy shows an exponential increase before entering into a saturation phase, and similar considerations apply also for the error in mass and in energy (with slightly better results for the simulation with lower time step size, as expected). This behaviour matches well with what has been previously reported in the literature for this problem.

## 7. Performance results

We now investigate the performance of the low-rank projector-splitting algorithms presented in Section 3. This, in particular, should highlight the efficiency of using our software framework `Ensign` and demonstrate that GPUs provide an efficient way to run such simulations.

To perform a comparison with the GPU outcomes, we present results on a dual-socket Intel Xeon Gold 6226R CPU based system with  $2 \times 16$  CPU cores and 192 GB of RAM. For parallelizing the CPU code OpenMP is used and the Intel MKL library is employed for matrix and vector operations. For the GPU performance results we use the NVIDIA card described at the beginning of Section 6, and cuBLAS for BLAS operations. All simulations are conducted in double precision arithmetics.

### 7.1. CPU/GPU comparison

We consider here the linear Landau problem (20) discretized with  $128^3$  points in both space and velocity variables. This is done so that the effort of the  $K$  and  $L$  step can be directly compared. We integrate the problem until final time  $T = 60$  with a time step size of  $\tau = 10^{-2}$  and rank  $r = 10$ . We report the timings (in descending order) of a single time step, for the relevant parts of the algorithms, in Table 1 and Table 2 for the first order and the second order schemes, respectively.

As expected, the most costly parts of the algorithms consist of the  $K$  and the  $L$  steps (with roughly the same computational time, as the degrees of freedom are equal in space and velocity). The cost of the  $S$  step, which involves the solution of a problem of size  $r \times r$  is negligible. The remaining major part of the cost lies in the computation of the  $C$  and

CPU		GPU	
	<i>Wall-clock time (s)</i>		<i>Wall-clock time (s)</i>
$K$ step	$2.87 \cdot 10^0$	$K$ step	$2.34 \cdot 10^{-2}$
$L$ step	$2.77 \cdot 10^0$	$L$ step	$2.34 \cdot 10^{-2}$
$D$ coefficients	$1.17 \cdot 10^0$	$D$ coefficients	$1.13 \cdot 10^{-2}$
$C$ coefficients	$1.17 \cdot 10^0$	$C$ coefficients	$1.12 \cdot 10^{-2}$
Electric field	$9.76 \cdot 10^{-2}$	QR decomposition $K$	$5.31 \cdot 10^{-3}$
QR decomposition $L$	$2.00 \cdot 10^{-2}$	QR decomposition $L$	$5.26 \cdot 10^{-3}$
QR decomposition $K$	$1.96 \cdot 10^{-2}$	Electric field	$2.39 \cdot 10^{-3}$
$S$ step	$6.72 \cdot 10^{-5}$	$S$ step	$7.43 \cdot 10^{-4}$
Total	$8.12 \cdot 10^0$	Total	$8.30 \cdot 10^{-2}$

Table 1: Breakdown of timings for a single step of the first order algorithm 1, in descending order, for CPU and GPU simulation of the linear Landau problem. The number of discretization points in both space and velocity is  $128^3$ , the final time is  $T = 60$ , the time step size is  $\tau = 10^{-2}$  and the rank is  $r = 10$ .

CPU		GPU	
	<i>Wall-clock time (s)</i>		<i>Wall-clock time (s)</i>
Lie splitting	$8.02 \cdot 10^0$	Lie splitting	$8.03 \cdot 10^{-2}$
First $K$ step + QR	$2.83 \cdot 10^0$	First $K$ step + QR	$3.19 \cdot 10^{-2}$
Second $K$ step + QR	$2.82 \cdot 10^0$	Second $K$ step + QR	$2.99 \cdot 10^{-2}$
$L$ step + QR	$2.82 \cdot 10^0$	$L$ step + QR	$2.89 \cdot 10^{-2}$
$C$ coefficients	$1.12 \cdot 10^0$	$C$ coefficients	$1.10 \cdot 10^{-2}$
$D$ coefficients	$1.11 \cdot 10^0$	$D$ coefficients	$1.09 \cdot 10^{-2}$
Electric field	$1.01 \cdot 10^{-1}$	Electric field	$1.53 \cdot 10^{-3}$
First $S$ step	$5.83 \cdot 10^{-5}$	First $S$ step	$6.81 \cdot 10^{-4}$
Second $S$ step	$5.12 \cdot 10^{-5}$	Second $S$ step	$6.50 \cdot 10^{-4}$
Total	$1.88 \cdot 10^1$	Total	$1.96 \cdot 10^{-1}$

Table 2: Breakdown of timings for a single step of the second order algorithm 2, in descending order, for CPU and GPU simulation of the linear Landau problem. The number of discretization points in both space and velocity is  $128^3$ , the final time is  $T = 60$ , the time step size is  $\tau = 10^{-2}$  and the rank is  $r = 10$ .

the  $D$  coefficients: again, this is expected, as they require a matrix-matrix product of size  $N_v \times r$  (and  $N_x \times r$ , respectively). A single time step of the second order scheme is, as we would expect, approximately twice as costly as the first order scheme.

In both cases, we observe a drastic speedup (up to a factor of 100) between the GPU and the CPU based systems. The main reason for this is that very efficient implementations of matrix-matrix products are available on the GPU (in particular, in cuBLAS). This helps both in computing the coefficients as well as performing the  $K$  and  $L$  step. In addition, our algorithm needs to compute transcendental functions in order to evaluate the matrix functions in Fourier space. This is also an area where the GPU kernels drastically outperform the corresponding CPU implementation.

## 7.2. Varying rank

We now investigate the performance of the GPU implementation for the second order low-rank projector-splitting algorithm for different ranks. For this purpose, we consider again the 6D linear Landau problem (20) with  $64^3$  discretization points for the spatial variables and  $128^3$  discretization points for the velocity ones.

We integrate the problem up to  $T = 60$  with a time step size of  $\tau = 10^{-2}$  and different ranks  $r = 5, 10, 15, 20$ . The computational times for a single time step of the simulation are reported in Table 3. First of all, we observe that the wall-clock time increases roughly in a linear fashion as the rank increases. This scaling is better than the theoretical estimates provided in Section 3.2.

	<i>Wall-clock time (s)</i>
Rank 5	$5.12 \cdot 10^{-2}$
Rank 10	$8.70 \cdot 10^{-2}$
Rank 15	$1.28 \cdot 10^{-1}$
Rank 20	$1.85 \cdot 10^{-1}$

Table 3: Timings of a single time step for the linear Landau problem with increasing ranks  $r$ . The second order dynamical low-rank algorithm 2 is employed. The number of discretization points in space is  $64^3$ , in velocity it is  $128^3$ , the final time is  $T = 60$  and the time step size is  $\tau = 10^{-2}$ .

Then, in Figure 6 we summarize the behavior of the electric energy, of the error in mass and in total energy for all the ranks considered. We can clearly observe that rank 5 is not enough for the 6D problem under investigation. Starting from rank 10, we see a substantial improvement, in particular in terms of decay of electric energy.

Finally, we repeat a similar experiment with the 6D two stream instability problem (21). In this case, we consider  $64^3$  discretization points for both spatial and velocity variables. The problem is then integrated up to  $T = 60$  with a time step size of  $\tau = 10^{-2}$  and increasing rank  $r = 5, 10, 15, 20$ . The computational times for a single time step are summarized in Table 4, and analogous conclusions as for the linear Landau simulations can be drawn. In terms of electric energy, error in mass and error in total energy, we collect the results in Figure 7. We note that for the linear regime rank 5 still gives very good results in that it

	<i>Wall-clock time (s)</i>
Rank 5	$1.84 \cdot 10^{-2}$
Rank 10	$3.06 \cdot 10^{-2}$
Rank 15	$4.85 \cdot 10^{-2}$
Rank 20	$7.15 \cdot 10^{-2}$

Table 4: Timings of a single time step for the two stream instability problem with increasing ranks  $r$ . The second order dynamical low-rank algorithm 2 is employed. The number of discretization points in both space and velocity is  $64^3$ , the final time is  $T = 60$  and the time step size is  $\tau = 10^{-2}$ .

perfectly predicts both the growth rate of the instability as well as the time of its onset. Starting at saturation the rank 5 solution tends to overestimate the electric energy and thus the rank has to be increased. In order to capture saturation a rank 10 simulation is sufficient. If it is desired to integrate far into the nonlinear regime the rank has to be increased further.

## 8. Conclusions

We have demonstrated, by conducting numerical simulations for two test problems, that six-dimensional Vlasov simulations using a projector-splitting dynamical low-rank algorithm can be efficiently run on GPU based systems. In particular, we report a drastic speedup compared to the CPU implementation, and we remark that these are the first dynamical low-rank results obtained for the full six-dimensional problem. We also emphasize that results with similar resolution using a direct (Eulerian or semi-Lagrangian) Vlasov solver could only be attained on large-scale supercomputers, while our simulations have been conducted on a single workstation equipped with an NVIDIA A100 card.

Algorithmic efficiency has been achieved by proposing a CFL-free and second order exponential integrator based dynamical low-rank scheme that uses a Fourier spectral phase space discretization. Implementation efficiency has been achieved by basing the implementation on the software framework **Ensign**.

## References

- [1] J. Bigot, V. Grandgirard, G. Latu, C. Passeron, F. Rozar, and O. Thomine. Scaling gysela code beyond 32K-cores on bluegene/Q. In *ESAIM: Proc.*, volume 43, pages 117–135. EDP Sciences, 2013.
- [2] H. Burau, R. Widera, W. Hönig, G. Juckeland, A. Debus, T. Kluge, U. Schramm, T.E. Cowan, R. Sauerbrey, and M. Bussmann. PIconGPU: A Fully Relativistic Particle-in-Cell Code for a GPU Cluster. *IEEE Trans. Plasma Sci.*, 38(10):2831–2839, 2010.
- [3] E. Camporeale, G.L. Delzanno, B.K. Bergen, and J.D. Moulton. On the velocity space discretization for the Vlasov–Poisson system: Comparison between implicit Hermite spectral and Particle-in-Cell methods. *Comput. Phys. Commun.*, 198:47–58, 2016.

- [4] G. Ceruti and C. Lubich. An unconventional robust integrator for dynamical low-rank approximation. *BIT Numer. Math.*, 62:23–44, 2021.
- [5] Intel Corporation. Intel Math Kernel Library. <https://software.intel.com/content/www/us/en/develop/tools/oneapi/components/onemkl> 2021.
- [6] NVIDIA Corporation. cuBLAS documentation. <https://docs.nvidia.com/cuda/cublas/index.htm> 2021.
- [7] Z. Ding, L. Einkemmer, and Q. Li. Dynamical Low-Rank Integrator for the Linear Boltzmann Equation: Error Analysis in the Diffusion Limit. *SIAM J. Numer. Anal.*, 59(4):2254–2285, 2021.
- [8] L. Einkemmer. High performance computing aspects of a dimension independent semi-Lagrangian discontinuous Galerkin code. *Comput. Phys. Commun.*, 202:326–336, 2016.
- [9] L. Einkemmer. A Low-Rank algorithm for Weakly Compressible Flow. *SIAM J. Sci. Comput.*, 41(5):A2795–A2814, 2019.
- [10] L. Einkemmer. A performance comparison of semi-Lagrangian discontinuous Galerkin and spline based Vlasov solvers in four dimensions. *J. Comput. Phys.*, 376:937–951, 2019.
- [11] L. Einkemmer, J. Hu, and Y. Wang. An asymptotic-preserving dynamical low-rank method for the multi-scale multi-dimensional linear transport equation. *J. Comput. Phys.*, 439:110353, 2021.
- [12] L. Einkemmer, J. Hu, and L. Ying. An Efficient Dynamical Low-Rank Algorithm for the Boltzmann-BGK Equation Close to the Compressible Viscous Flow Regime. *SIAM J. Sci. Comput.*, 43(5):B1057–B1080, 2021.
- [13] L. Einkemmer and I. Joseph. A mass, momentum, and energy conservative dynamical low-rank scheme for the Vlasov equation. *J. Comput. Phys.*, 443:110495, 2021.
- [14] L. Einkemmer and C. Lubich. A Low-Rank Projector-Splitting Integrator for the Vlasov–Poisson Equation. *SIAM J. Sci. Comput.*, 40(5):B1330–B1360, 2018.
- [15] L. Einkemmer and A. Ostermann. An almost symmetric Strang splitting scheme for nonlinear evolution equations. *Comput. Math. with Appl.*, 67(12):2144–2157, 2014.
- [16] L. Einkemmer and A. Ostermann. An almost symmetric Strang splitting scheme for the construction of high order composition methods. *J. Comput. Appl. Math.*, 271:307–318, 2014.
- [17] L. Einkemmer, A. Ostermann, and C. Piazzola. A low-rank projector-splitting integrator for the Vlasov–Maxwell equations with divergence correction. *J. Comput. Phys.*, 403:109063, 2020.

- [18] V. Grandgirard, Y. Sarazin, X. Garbet, G. Dif-Pradalier, P. Ghendrih, N. Crouseilles, G. Latu, E. Sonnendrücker, N. Besse, and P. Bertrand. GYSELA, a full- $f$  global gyrokinetic Semi-Lagrangian code for ITG turbulence simulations. In *AIP Conf. Proc.*, volume 871, pages 100–111. American Institute of Physics, 2006.
- [19] W. Guo and Y. Cheng. A Sparse Grid Discontinuous Galerkin Method for High-Dimensional Transport Equations and Its Application to Kinetic Simulations. *SIAM J. Sci. Comput.*, 38(6):A3381–A3409, 2016.
- [20] W. Guo and J.-M. Qiu. A low rank tensor representation of linear transport and non-linear Vlasov solutions and their associated flow maps. *J. Comput. Phys.*, 458:111089, 2022.
- [21] M. Hochbruck and A. Ostermann. Exponential integrators. *Acta Numer.*, 19:209–286, 2010.
- [22] O. Koch and C. Lubich. Dynamical Low-Rank Approximation. *SIAM J. Matrix Anal. Appl.*, 29(2):434–454, 2007.
- [23] K. Kormann. A Semi-Lagrangian Vlasov Solver in Tensor Train Format. *SIAM J. Sci. Comput.*, 37(4):B613–B632, 2015.
- [24] K. Kormann and E. Sonnendrücker. Sparse Grids for the Vlasov–Poisson Equation. In *Sparse Grids and Applications - Stuttgart 2014*, volume 109, pages 163–190. Springer International Publishing, 2016.
- [25] J. Kusch, G. Ceruti, L. Einkemmer, and M. Frank. Dynamical low-rank approximation for Burgers’ equation with uncertainty. *arXiv:2105.04358*, 2021.
- [26] J. Kusch, L. Einkemmer, and G. Ceruti. On the stability of robust dynamical low-rank approximations for hyperbolic problems. *arXiv:2107.07282*, 2021.
- [27] C. Lubich. *From Quantum to Classical Molecular Dynamics: Reduced Models and Numerical Analysis*. European Mathematical Society, 2008.
- [28] C. Lubich and I.V. Oseledets. A projector-splitting integrator for dynamical low-rank approximation. *BIT Numer. Math.*, 54:171–188, 2014.
- [29] H.-D. Meyer, F. Gatti, and G.A. Worth. *Multidimensional Quantum Dynamics: MCTDH Theory and Applications*. Wiley-VCH, 2009.
- [30] H.-D. Meyer, U. Manthe, and L.S. Cederbaum. The multi-configurational time-dependent Hartree approach. *Chem. Phys. Lett.*, 165(1):73–78, 1990.
- [31] R. Nath, S. Tomov, and J. Dongarra. Accelerating GPU Kernels for Dense Linear Algebra. In *High Performance Computing for Computational Science – VECPAR 2010*, volume 6449, pages 83–92. Springer Berlin Heidelberg, 2011.

- [32] Z. Peng and R.G. McClarren. A high-order/low-order (HOLO) algorithm for preserving conservation in time-dependent low-rank transport calculations. *J. Comput. Phys.*, 447:110672, 2021.
- [33] Z. Peng, R.G. McClarren, and M. Frank. A low-rank method for two-dimensional time-dependent radiation transport calculations. *J. Comput. Phys.*, 421:109735, 2020.
- [34] The SeLaLib project team. SeLaLib library. <https://selalib.github.io/>, 2021.
- [35] D. Tskhakaya and R. Schneider. Optimization of PIC codes by improved memory management. *J. Comput. Phys.*, 225(1):829–839, 2007.
- [36] J.P. Verboncoeur. Particle simulation of plasmas: review and advances. *Plasma Phys. Control. Fusion*, 47(5A):A231–A260, 2005.
- [37] S. von Alfthan, D. Pokhotelov, Y. Kempf, S. Hoilijoki, I. Honkonen, A. Sandroos, and M. Palmroth. Vlasiator: First global hybrid-Vlasov simulations of Earth’s foreshock and magnetosheath. *J. Atmos. Sol. Terr. Phys.*, 120:24–35, 2014.
- [38] Z. Xianyi, W. Qian, and Z. Yunquan. Model-driven Level 3 BLAS Performance Optimization on Loongson 3A Processor. In *2012 IEEE 18th international conference on parallel and distributed systems*, pages 684–691. IEEE, 2012.

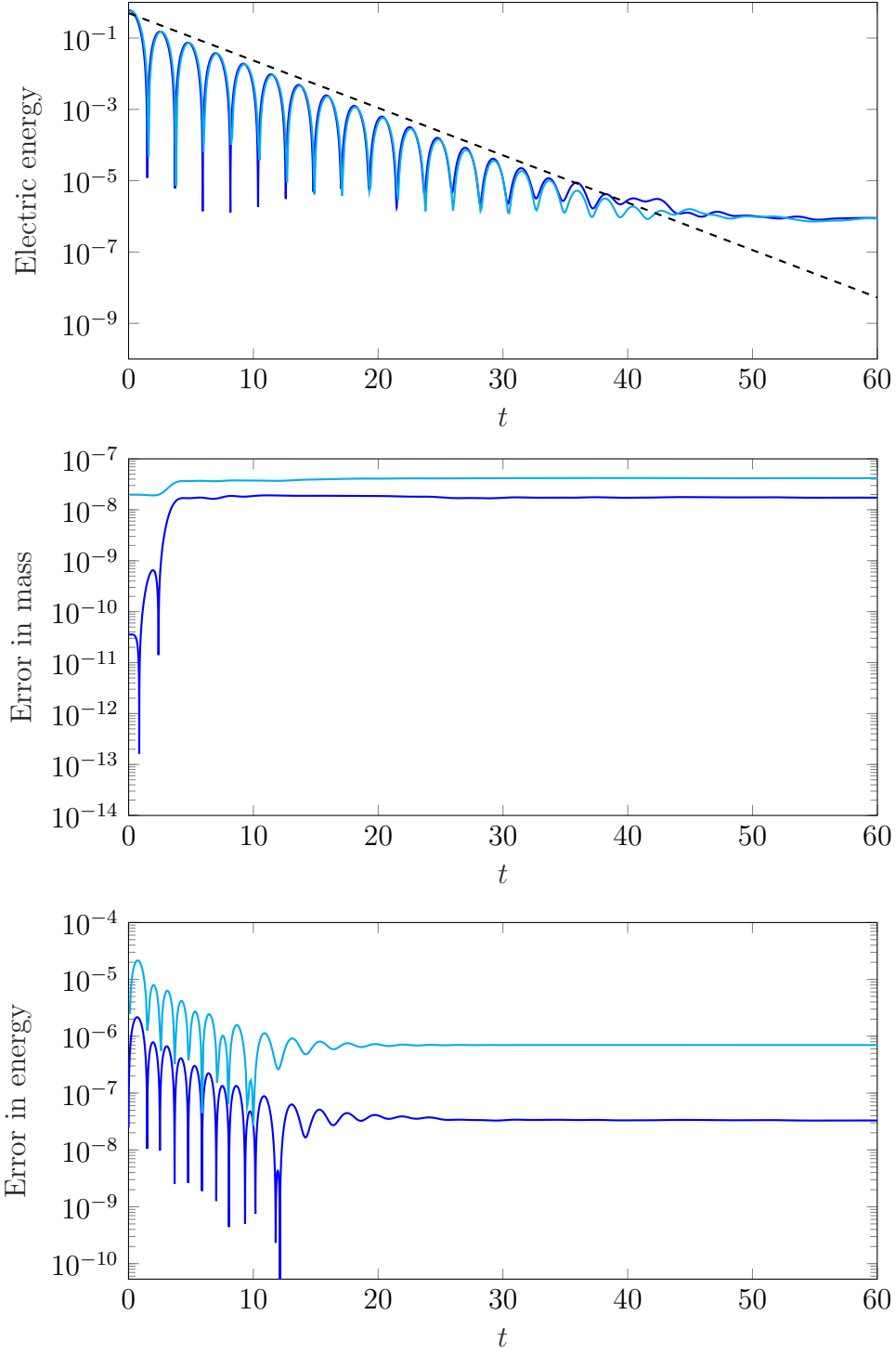


Figure 4: Linear Landau simulation with  $64^3$  space discretization points,  $256^3$  velocity discretization points, final time  $T = 60$ , rank  $r = 10$  and time step sizes  $\tau = 10^{-1}$  (cyan line) and  $\tau = 10^{-2}$  (blue line), see Section 6.2. The second order low-rank projector-splitting algorithm 2 is employed. Top plot: behavior of electric energy, with reference decay rate. Center plot: error in mass (relative). Bottom plot: error in total energy (relative).



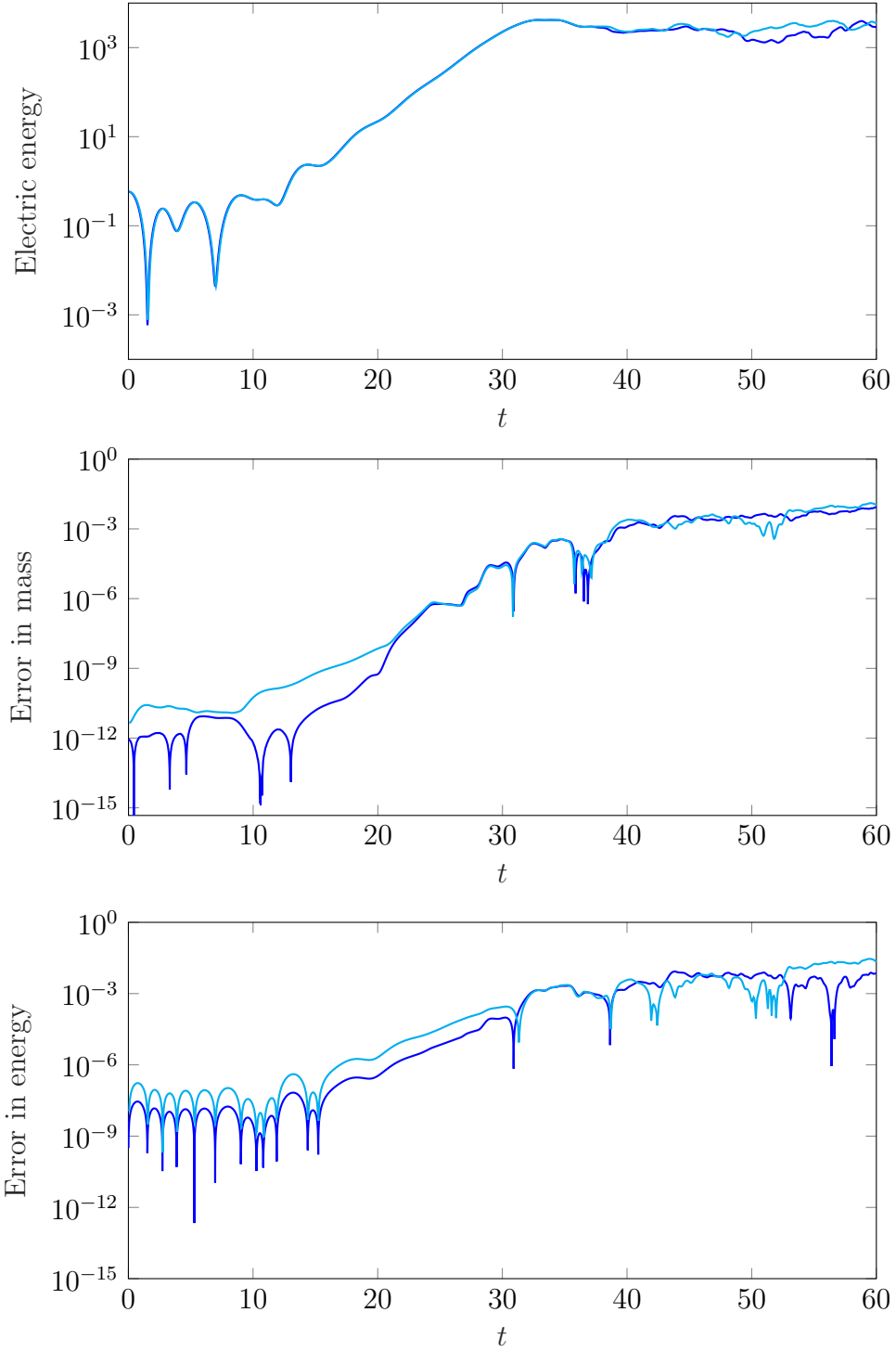


Figure 5: Two stream instability simulation with  $128^3$  discretization points for both space and velocity, final time  $T = 60$ , rank  $r = 10$  and time step sizes  $\tau = 6 \cdot 10^{-2}$  (cyan line) and  $\tau = 10^{-2}$  (blue line), see Section 6.3. The second order low-rank projector-splitting algorithm 2 is employed. Top plot: behavior of electric energy. Center plot: error in mass (relative). Bottom plot: error in total energy (relative).

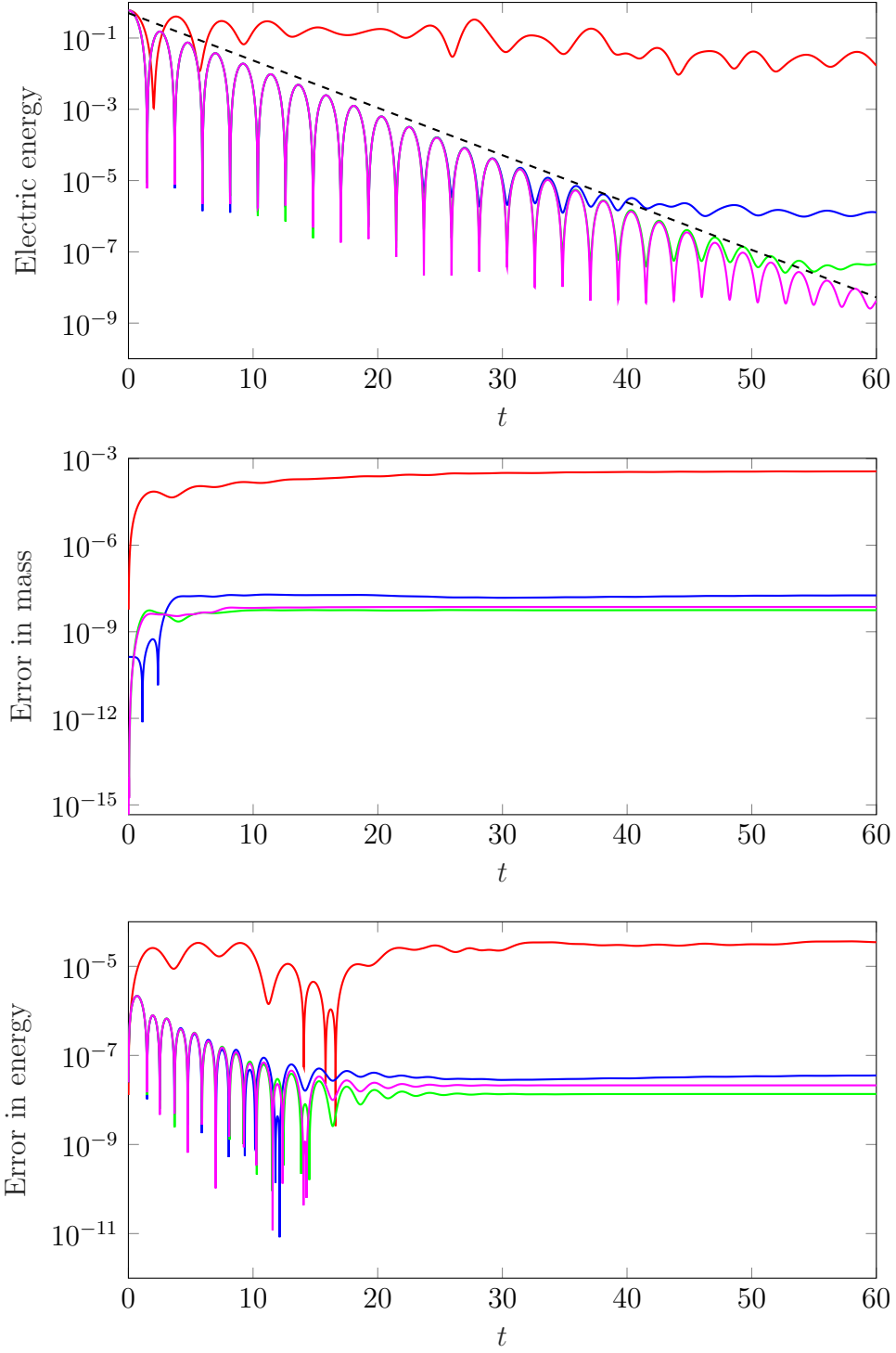


Figure 6: Linear Landau simulation with  $64^3$  space discretization points,  $128^3$  velocity discretization points, final time  $T = 60$ , time step size  $\tau = 10^{-2}$  and different ranks  $r$ , see Section 7.2. The second order low-rank projector-splitting algorithm 2 is employed. The red line corresponds to  $r = 5$ , the blue one to  $r = 10$ , the green one to  $r = 15$  and the magenta one to  $r = 20$ . Top plot: behaviour of electric energy, with reference decay rate. Center plot: error in mass (relative). Bottom plot: error in total energy (relative).

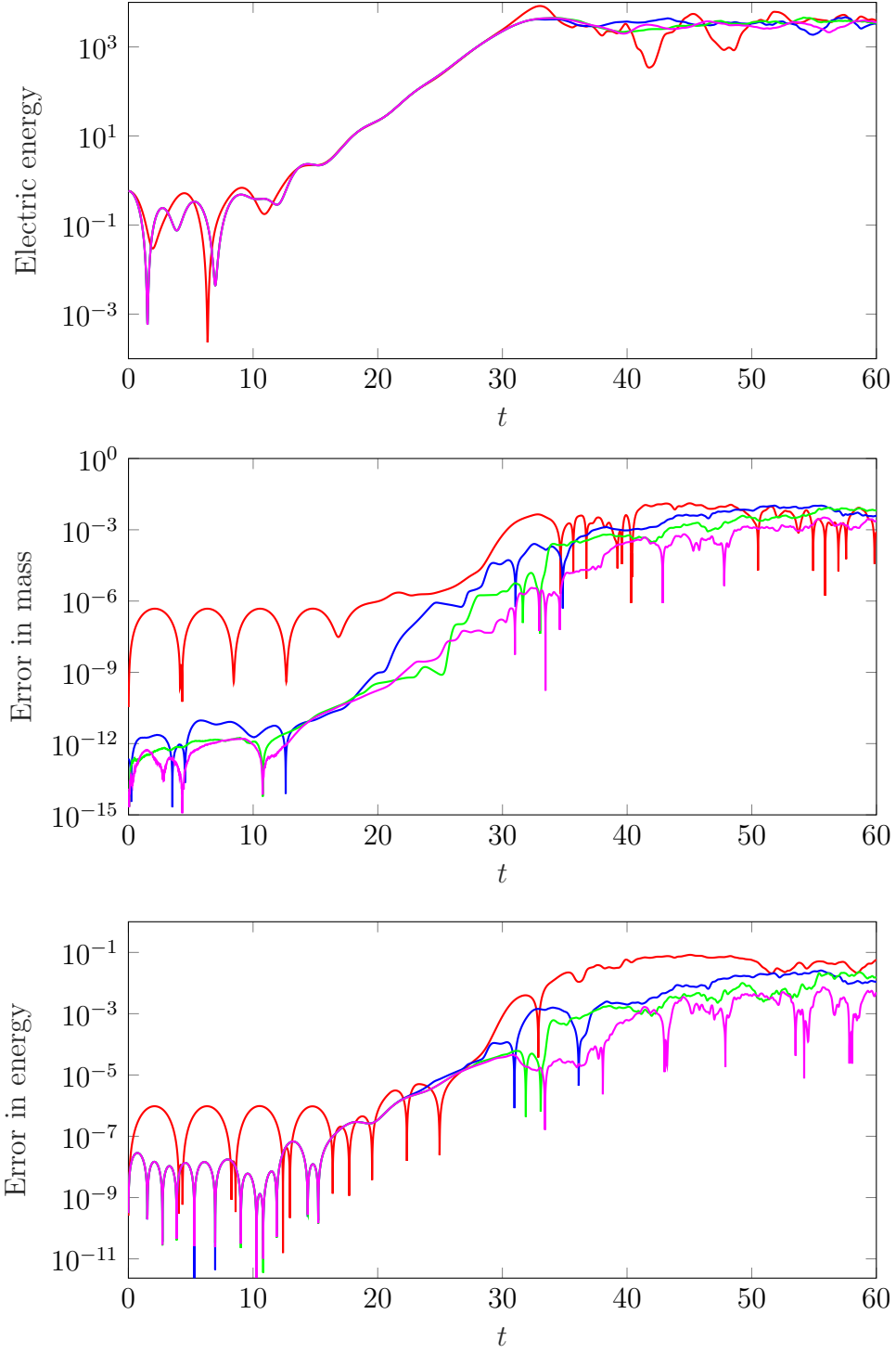


Figure 7: Two stream instability simulation with  $64^3$  discretization points for both space and velocity, final time  $T = 60$ , time step size  $\tau = 10^{-2}$  and different ranks  $r$ , see Section 7.2. The second order low-rank projector-splitting algorithm 2 is employed. The red line corresponds to  $r = 5$ , the blue one to  $r = 10$ , the green one to  $r = 15$  and the magenta one to  $r = 20$ . Top plot: behaviour of electric energy. Center plot: error in mass (relative). Bottom plot: error in total energy (relative).